Performance of the antisymmetrized molecular dynamics transport model for low energy reactions: Comparison with experimental results for ^{18}O + ^{12}C at 16.7 MeV/nucleon

L. Baldesi [1,2,*] S. Barlini [1,2] A. A. Stefanini [1,2] A. Camaiani [1,2] S. Piantelli [2] G. Casini [2] C. Ciampi [3]
M. Cinausero [4] M. Cicerchia [5] D. Dell'Aquila [6,7] L. Domenichetti [8] D. Fabris [9] C. Frosin [1,2] A. Gozzelino [4]
I. Lombardo [10,11] T. Marchi [4] S. Moretto [5,9] A. Mengarelli [12] A. Olmi [2] G. Pasquali [1,2] L. Scomparin [13]
S. Valdré [2] and E. Vanzan [5,9]

[1]*Dipartimento di Fisica, Università di Firenze, I-50019 Sesto Fiorentino, Italy*
[2]*INFN Sezione di Firenze, I-50019 Sesto Fiorentino, Italy*
[3]*Grand Accélérateur National d'Ions Lourds (GANIL), CEA/DRF–CNRS/IN2P3, Boulevard Henri Becquerel, F-14076 Caen, France*
[4]*INFN Laboratori Nazionali di Legnaro, 35020 Legnaro, Italy*
[5]*Dipartimento di Fisica, Università di Padova, I-35121 Padova, Italy*
[6]*Dipartimento di Fisica "Ettore Pancini", Università di Napoli Federico II, I-80126 Napoli, Italy*
[7]*INFN Sezione di Napoli, 80126 Napoli, Italy*
[8]*Institut Laue-Langevin, 71 Av, des Martyrs, Grenoble 38000, France*
[9]*INFN Sezione di Padova, 35131 Padova, Italy*
[10]*INFN Sezione di Catania, 95123 Catania, Italy*
[11]*Dipartimento di Fisica e Astronomia, Università di Catania, 95123 Catania, Italy*
[12]*INFN Sezione di Bologna, I-40127 Bologna, Italy*
[13]*Karlsruher Institut für Technologie, Kaiserstraße 12, 76131 Karlsruhe, Deutschland*

The charged particles produced in the ^{18}O + ^{12}C reaction at 16.7 MeV/nucleon have been detected using the GARFIELD+RCo apparatus at Laboratori Nazionali di Legnaro and compared with the transport code antisymmetrized molecular dynamics (AMD) followed by GEMINI++ as afterburner. To our knowledge, it is the first time that this model is applied to a nuclear reaction between light nuclei at so relatively low bombarding energy. The general agreement between experimental data and model is very good for fragments with $Z \geqslant 10$, assuming a fusion process source, and for intermediate fragments ($Z = 3, 4$). A discrepancy in the relative cross section of the different reaction mechanisms has been pointed out for fragments with $4 < Z < 10$ as the model seems to produce less dissipative reactions.

I. INTRODUCTION

The main characteristics of nuclear reactions are strongly dependent on two parameters: the bombarding energy and the centrality of the reaction. It is well known that at low beam energy (below ≈ 10 MeV/nucleon) the complete fusion is the main reaction channel for central collisions between nuclei with moderate size, almost exhausting the total reaction cross section [1]. The complete fusion mechanism is characterized by the formation of a compound nucleus and its following decay, which is globally well described by the statistical decay model based on the Hauser-Feshbach formalism [2].

At higher energy, between 20–80 MeV/nucleon, in central collisions the complete fusion is gradually replaced by the incomplete one, where nucleons or clusters escape from the system well before the thermalization. Moreover, for less central collisions, at those energies the cross section is dominated by the binary output, characterized by the presence of two main fragments, the so-called quasiprojectile (QP) and quasitarget (QT), which also decay as a result of their excitation during the contact phase. In the overlapping region between them, depending on the size of the system and the bombarding energy, another structure, usually called the "neck", can be formed during the collision. The study of the isotopic content of fragments generated in the decay of the neck structure is of particular interest for the investigation of the isospin transport mechanism [3,4].

We present here the results of the study of the reaction ^{18}O + ^{12}C at 16.7 MeV/nucleon, for which the pure complete fusion scenario is not fully representative. Indeed, from the systematics in the literature [5–8], we can estimate the fraction of the fusion cross section with respect to the total reaction cross section foreseen in our reaction: considering the corresponding $E_{c.m.}/A = 4$ MeV/nucleon, the systematics [7] predicts the fusion cross section to be around 17% of the total one, shared between complete (11%) and incomplete (6%) fusion, while in [8] a 15.5% of complete fusion is expected. Therefore, a large fraction of the reaction cross section cannot be accounted for by a complete fusion process well

*Contact author: lucia.baldesi@fi.infn.it

described by the statistical codes and a different theoretical approach should be applied. In the literature, at bombarding energy similar to our system, a transport model has been used in [9], where the $^{32}S + ^{40,48}Ca$ at 17.7 MeV/nucleon reactions have been analyzed. In that work, where a clear isospin diffusion effect was observed in peripheral binary events, a comparison was attempted between the experimental data and the TWINGO [10] model, based on the stochastic mean field approach, coupled with GEMINI++ [11,12] as afterburner. A similar study was proposed in [13] using the $^{86}Kr + ^{64,58}Ni$ and $^{124,112}Sn$ massive reactions at 15 and 25 MeV/nucleon. Experimental results were compared with previous experimental data on the lighter system $^{40}Ar + ^{64,58}Ni$ at 15 MeV/nucleon and with the constrained molecular dynamics (CoMD) model [14,15].

In this paper, we want to stress and test the antisymmetrized molecular dynamics (AMD) model [16], coupled with GEMINI++ as afterburner, outside its typical application range, stated in literature. Indeed, AMD has been shown to successfully reproduce the main features of many intermediate mass systems with energy in the range of 25–100 MeV/nucleon [3,17–19]. In [20–24] this code has been tested with success also for light systems (13–40 nucleons) such as C+H, C+C, S+C, and Ne+C with energies from 25 to 95 MeV/nucleon, also highlighting the importance of the clustering processes [25]. Here, the fragment properties will be used as a benchmark to validate the use of the AMD model below its typical energy range. To our knowledge, it is the first time that this model is applied at so relatively low energy (below 20 MeV/nucleon), with a so light a system (below 30 nucleons).

The paper is organized as follows. The experimental apparatus and the simulation code are described in Sec. II. The data analysis and results are discussed in Sec. III, while our conclusions are summarized in Sec. IV.

II. EXPERIMENTAL APPARATUS AND THEORETICAL MODEL

The experiment was performed at the Laboratori Nazionali di Legnaro (LNL, Italy). A pulsed beam of ^{18}O at 300 MeV delivered by the ALPI Linac with an average current of 0.1 pnA impinging on a ^{12}C target with a thickness of 70 μg/cm^2 was used. Data were collected with the GARFIELD+RCo array [26]. The apparatus is characterized by a geometrical efficiency of almost 80% of the total solid angle and a good granularity including almost 300 ΔE-E telescopes. GARFIELD is dedicated to the detection of light charged particles (LCPs) and intermediate mass fragments (IMFs), while the RCo is aimed at the detection of the heavier fragments, such as the evaporation residues, as well as the LCPs and IMFs emitted within its solid angle. The RCo detector is placed at forward angles covering the angular range $5° < \theta < 17°$. It is an array of three-stage telescopes including an ionization chamber (IC), divided into eight sectors, followed by 300 μm thick silicon strip detectors (eight strips for each sector) and CsI(Tl) crystals as the last stage (six scintillators for each sector, read out by photodiodes). Two techniques can be used for particle identification: the ΔE-E
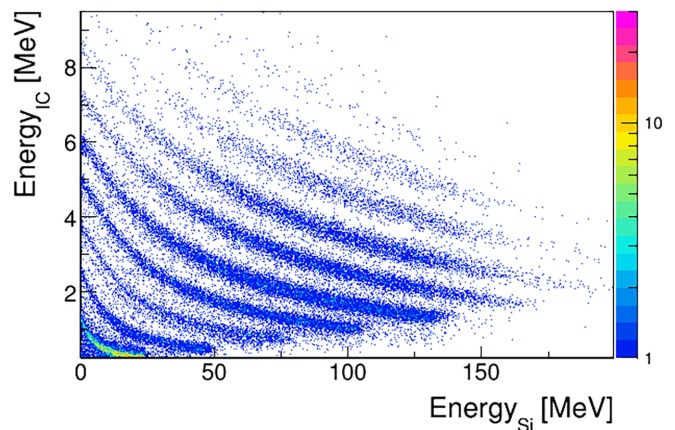

FIG. 1. ΔE-E correlation "IC energy vs Si energy" in the RCo apparatus. The lines correspond to ions from $Z = 2$ up to $Z = 10$.

technique and the pulse shape analysis (PSA). The reaction products with $Z > 1$ stopped in a RCo Si can be identified in charge by the ΔE-E correlation "IC vs Si" (an example is shown in Fig. 1), with a very low energy threshold ($\approx$0.5–1 MeV/nucleon). Moreover, the particles above an energy threshold of 3–5 MeV/nucleon stopped in the silicon detectors can be identified in charge and, in a more limited energetic region, also in mass with the PSA (see Fig. 2), with an energy resolution of about 1%. In this experiment, we adopted the maximum of the current signal in the RCo as the best Si-PSA parameter, according to the results of the research and development of the FAZIA collaboration [27]. In fact, a suitable upgrade of the front-end electronics allowed to program the on-board field programmable gate array (FPGA) [28] in order to compute the derivative of the charge signal, obtaining the on-line evaluation of the current maximum. The isotopic resolution with this technique is achieved up to $Z = 10$ for at least a limited zone of energy (red contour in Fig. 2). For those products identified only in charge Z, the most probable mass value is assigned according to the theoretical model. Finally, particles punching through the silicon stage are identified in charge and mass with the ΔE-E
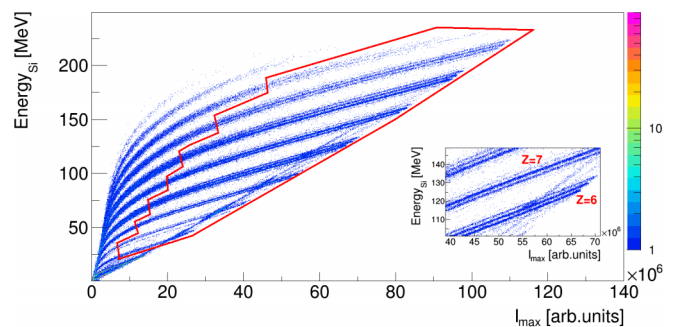

FIG. 2. PSA correlation "energy vs current maximum" for a silicon detector of the RCo. The charge identification is achieved for all ions, up to $Z = 12$. The red contour delimits the region where the mass identification is obtained. The inset shows a close up of the $Z = 6,7$ region, where the mass-discrimination capability for these elements can be clearly seen.

correlation "Si vs CsI(Tl)" and, up to $Z = 3$, with the PSA method in CsI(Tl) scintillators, through the use of the fast vs. slow correlation.

GARFIELD is a two-stage detector with azimuthal symmetry consisting of two microstrip gas chambers and 180 CsI(Tl) scintillators (arranged in eight rings), readout by photodiodes, and it covers the polar range from $30°$ to $150°$. The particles detected in GARFIELD are identified in charge using the ΔE-E correlation "microstrip vs CsI(Tl)" with an energy resolution of 5% and an energy threshold of ≈ 1 MeV/nucleon. In our experiment, the GARFIELD apparatus detects mainly LCPs and so the identification both in charge and mass of particles up to $Z = 3$ with an energy threshold of ≈ 2–4 MeV/nucleon is obtained using the PSA method in the CsI(Tl) scintillators. A more complete description of the experimental apparatus and its performances can be found in [26].

As anticipated, in this paper we adopt the AMD [16] transport model, which belongs to the quantum molecular dynamics (QMD) family. The time evolution of a system of nucleons is described by means of the Slater determinant of a Gaussian wave packets, representing the state of the system at each time step. The equation of motion of the system is then obtained applying a time-dependent variational principle. In the Hamiltonian, an effective interaction of Skyrme type (SLy4 of Ref. [29]) is included. For this light system at low bombarding energy, the density variations during the collisions should be small and thus also the stiffness of the symmetry energy is expected to have a negligible role. Therefore, we have used the soft symmetry energy parametrization (slope parameter $L = 46$ MeV), which is the standard of AMD, assuming for the normal density term S_0 the standard value of 32 MeV [30]. Two-nucleon collisions are taken into account as stochastic transitions among AMD states, under the constraint of momentum and energy conservation and the strict observance of the Pauli principle, with a transition probability depending on the in-medium NN cross section. In this work we used the parametrization introduced in [31], with the standard value $y = 0.85$. The reaction calculation has been stopped for each event after 500 fm/c, a time at which the dynamical phase is safely concluded [17]. About 1.3×10^5 events were produced in the whole impact parameter range up to the grazing value (8 fm), with a triangular probability distribution. The chosen number is a compromise between the need to describe with sufficient statistics the various reaction channels and the CPU calculation time. At the end of the dynamical phase, the excited fragments are allowed to decay towards the ground state; this evaporation phase is modeled via the afterburner (GEMINI++), producing 1000 events for each primary one.

Before comparison with the experimental data, the simulated events were filtered through a software replica of the apparatus, which reproduces the detection conditions such as geometry, energy thresholds, and energy resolution. Also the mass assignment for fragments with $Z < 11$ exactly follows the same experimental conditions: only for particles with energy above the mass identification threshold in silicon PSA do we keep their original mass. Below such identification limit, the theoretical fixed mass is assigned.
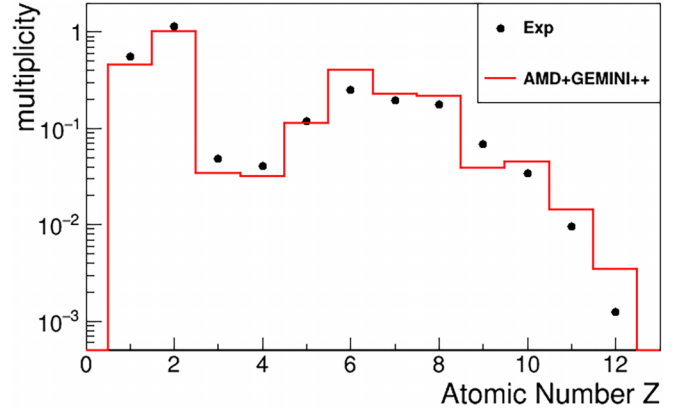

FIG. 3. Charge multiplicity distributions. Black dots are the experimental data and the red line represents the AMD+GEMINI++ result. The distributions are normalized to their number of events.

III. EXPERIMENTAL RESULTS AND ANALYSIS

As a first step of our analysis, we select only events where a significant part of the total ejectiles has been experimentally identified.

In particular, we use the conditions $5 < Z_{\text{tot}} < 15$ and $0.3 < p_{\text{tot}}/p_{\text{beam}} < 1.1$. A condition on the multiplicity of particles is also introduced to avoid events of elastic scattering: we consider only events with charge particle multiplicity greater than one. Starting from the initial statistics of 2×10^7 and 1×10^8 events, the applied conditions select 32% and 40% for the experimental and the model data, respectively.

The fragment charge distributions are presented in Fig. 3 for the experimental data and the model simulation. Each distribution is normalized to its number of events. The black dots represent the experimental data, while the red lines are the AMD+GEMINI++ results. Statistical errors are smaller than the marker size. The simulation code reproduces very well the experimental values, though some sizable differences are present for $Z = 6, 9, 12$.

In Fig. 4, the correlation plots between the charge Z and the laboratory velocity component along the beam axis are shown. Again, each panel is normalized to its number of events. Panel
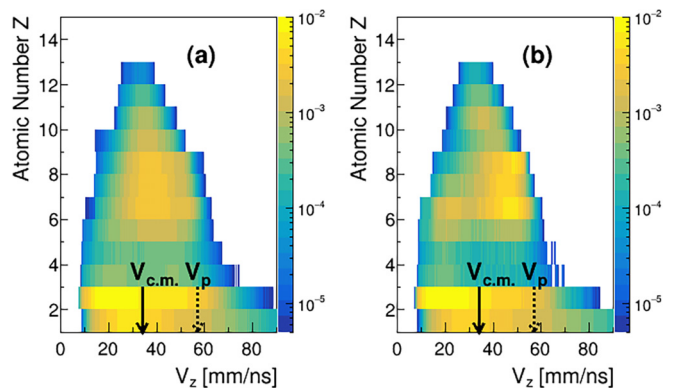

FIG. 4. Correlation of charge Z vs laboratory velocity along the beam axis. (a) Experimental data, (b) AMD+GEMINI++ predictions. The distributions are normalized to their integrals.
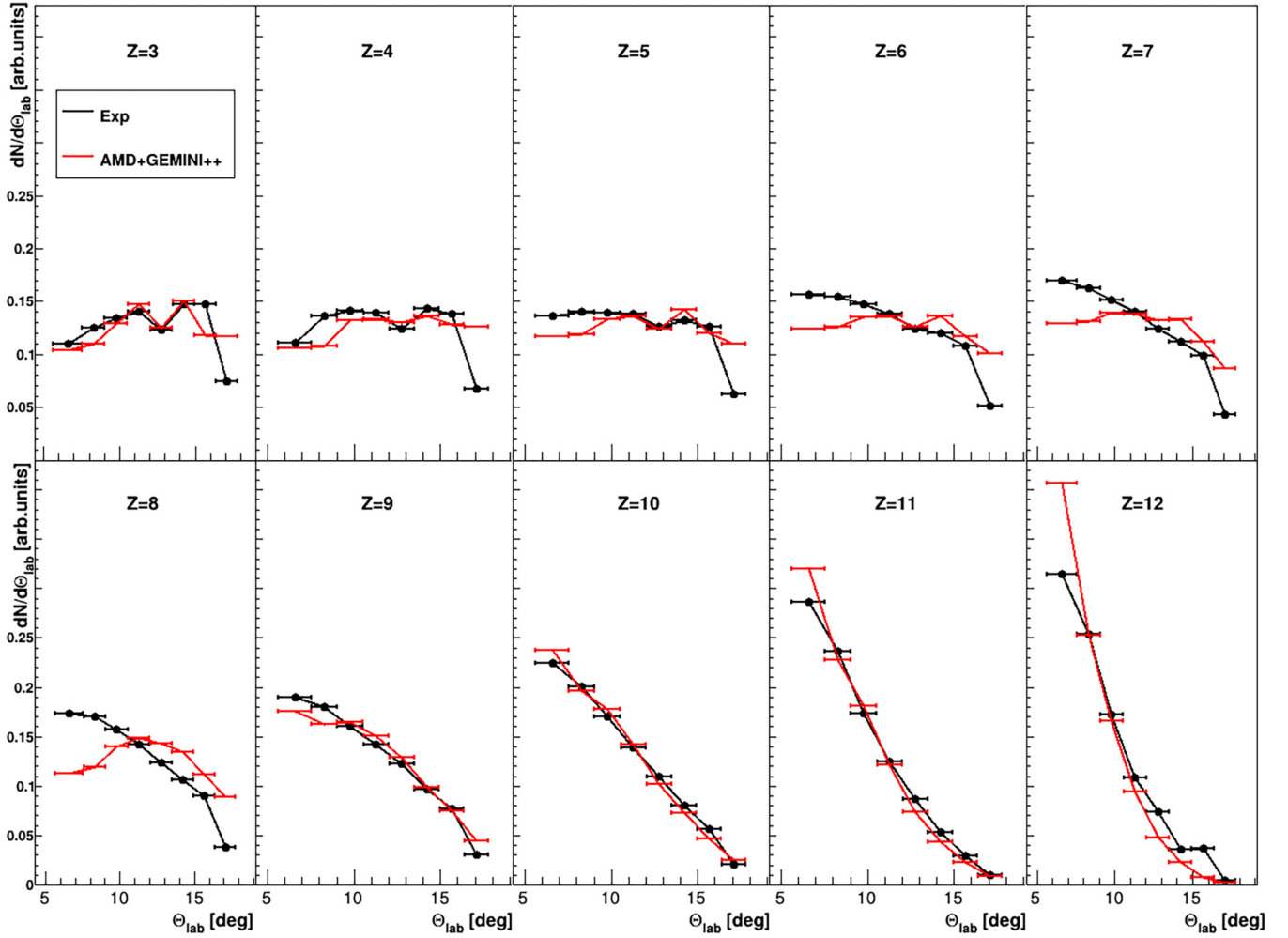
FIG. 5. Angular distributions of fragments ($Z > 2$) detected in the RCo apparatus. Black markers are the experimental distributions, while the red ones represent the AMD+GEMINI++ code.

(a) displays the experimental data, where the heavy fragments ($Z > 5$) are characterized by a wide velocity distribution between the compound nucleus velocity ($v_{CM} = 34.1$ mm/ns, solid arrow) and the beam velocity ($v_p = 56.8$ mm/ns, dashed arrow). The AMD+GEMINI++ correlation, shown in panel (b), exhibits characteristics similar to the experimental one, confirming that it can predict a broad range of reaction mechanisms as a function of the impact parameter, from central collisions, where complete (or incomplete) fusion can occur, to more peripheral collisions, where the binary scenario is the most probable. Looking at Fig. 4, the code correlation seems to present different relative weights between those two components, with the second one more populated.

In the following, we will focus on fragments with $Z > 2$. These particles have an angular distribution which is peaked at forward angles. Therefore, we select fragments detected in the RCo apparatus which allows for better angular, energy and mass resolution.

Exploiting the relatively good polar angle ($\pm 0.76°$) of the RCo silicon strip detectors, we can compare for each fragment of interest the angular distribution, as shown in Fig. 5, where the results for experimental data (black) and

AMD+GEMINI++ (red) are shown normalized to their area for a clearer shape comparison. Looking at Fig. 5, we can identify different zones with different behaviors. For the heavier products $Z \geqslant 9$, the angular distributions of both the experimental and AMD+GEMINI++ data are strongly peaked at small angles. This can suggest the origin of such fragments mainly as the evaporation residues resulting after a process of complete (incomplete) fusion. For these heavy products the model well reproduces the angular distributions. The scenario is different looking at the fragments with $5 < Z < 9$. As expected, the lighter the fragment, the smaller the probability of a residue to come from central events, being the distributions less peaked at small angles as the charge of the selected fragment decreases. Such a trend is not reproduced by AMD, which favors less dissipative events than fusion-like ones. Lighter ions, ($2 < Z < 6$), could be produced at the end of long decay chain ($Z = 5$) or emitted from the hot peripheral or central source ($Z = 3, 4$) [18,32]. AMD+GEMINI nicely reproduces the trends.

To better investigate how AMD+GEMINI++ is able to reproduce our experimental data, in Fig. 6 the velocity distributions for these fragments are shown. Once more, the
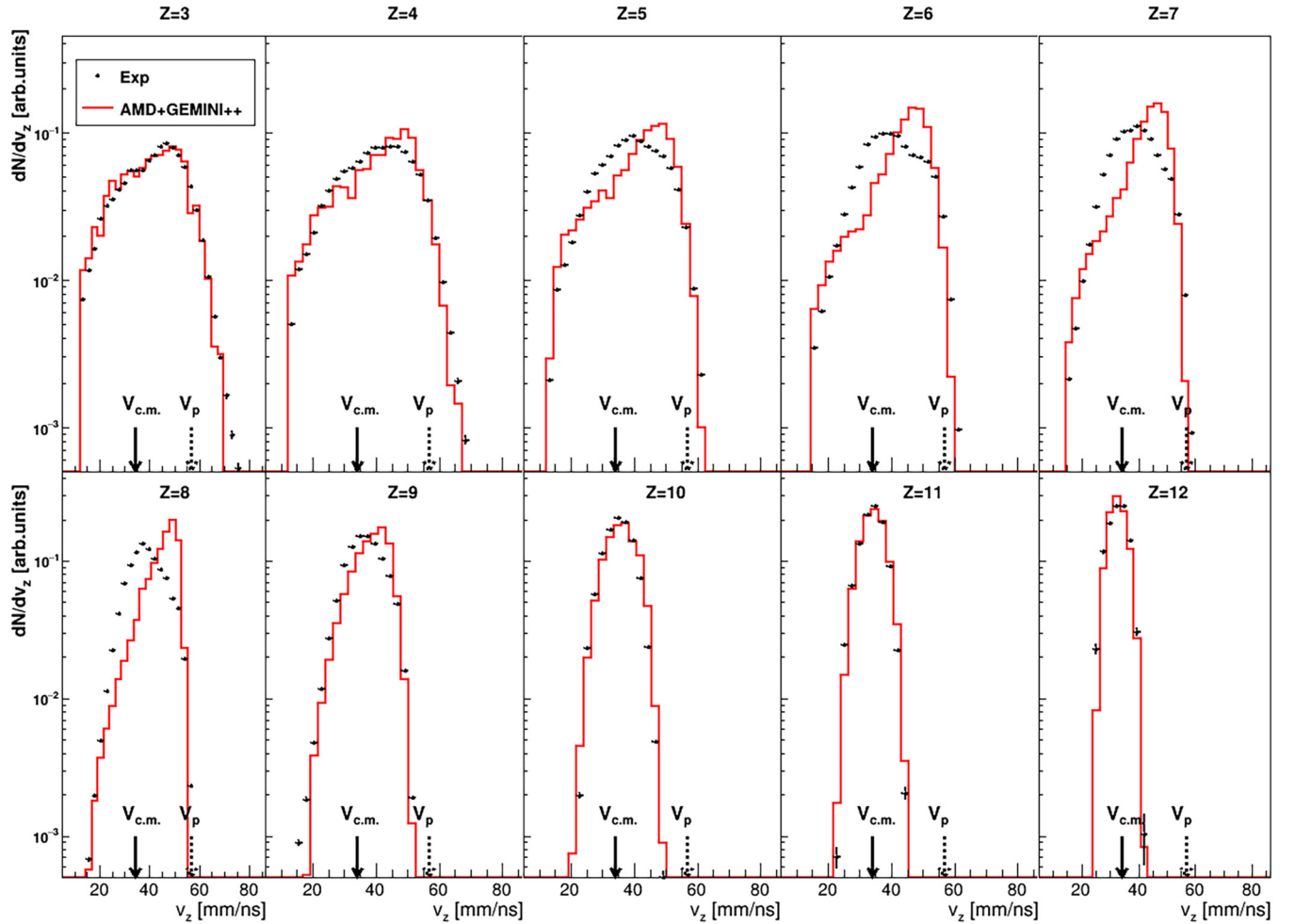
FIG. 6. Laboratory velocity (beam axis component) distributions for fragments with $Z > 2$. Black dots are the experimental distributions, and red lines represent the AMD+GEMINI++ results. The experimental and simulated distributions are normalized to the unitary area.

distributions are normalized to their integral for an easier shape comparison. Experimental (simulated) data are shown as black markers (red lines) including the statistical error bars, when visible. As already evident in Fig. 4, the AMD+GEMINI++ velocity distributions, despite some discrepancies in shape, cover the same velocity range of the experimental ones. Here, looking at $Z = 6$ and $Z = 8$ in particular, we can see the confirmation, on the velocity phase-space, of the tendency of AMD to unfavor dissipative events, as already highlighted by the angular distributions. It is worth mentioning that this is an opposite trend with respect to what observed for heavier systems [17–19,33] where the model turned out to favour more dissipative events in binary peripheral reactions.

The spectra with $Z \geqslant 10$ are of particular interest: the experimental spectra are peaked close to v_{CM} and they are very well reproduced by the AMD+GEMINI++ simulation. Considering that our system is characterized by $Z_{tot} = 14$ and $Z_{proj} = 8$, those heaviest fragments should be generated through a complete or incomplete fusion mechanism. The origin of such fragments is supported by the AMD model. In fact, in the following, we want to discuss, within the model, the primary sources in AMD that produce the observed final

(secondary) fragments velocity spectra of Fig. 6. We consider the primary fragments at 500 fm/c, being aware that particle emission can occur even before this time within AMD, whatever its nature, statistical or dynamical [34]. In Fig. 7 the velocity spectra (solid lines) for the three heavier residues $Z = 10$, 11, 12 are shown together with the contributions to these spectra due to different primary fragments (dashed lines). The total spectra area is normalized to unit area. The velocity distribution of a fragment coming from a complete fusion, i.e., a primary fragment $Z = 14$ (gray dashed line), is a Gaussian centered at v_{CM}, as expected. By decreasing the atomic number of the primary fragment, the distribution of the secondary fragments shifts at higher velocities and the shape becomes less Gaussian. For example, for a secondary fragment $Z = 10$ coming from a primary fragment with the same atomic number (blue line) the distribution is peaked at velocities greater than v_{CM}.

We now move to comment the lightest fragments ($Z = 3$, 4), whose various features are rather well reproduced by AMD (Figs. 3, 5, and 6). By repeating the study on the origin of the secondary fragments, one obtains Fig. 8 that displays the total spectra (solid lines) and the spectra for some different primary fragments (dashed lines) that lead to the final secondary IMF.
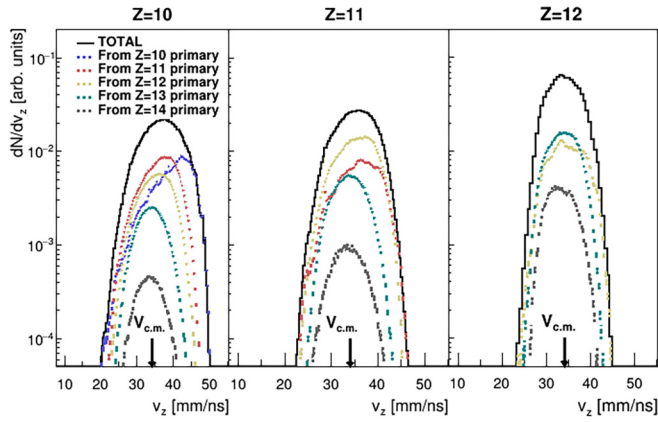
FIG. 7. Model data: laboratory velocity (beam axis component) distributions for secondary fragments with $Z = 10, 11, 12$. The total velocity spectra, normalized to unit area, are shown in black solid lines, while colored dashed lines represent the velocity distributions with primary fragment selection.

FIG. 9. Model data: laboratory velocity (beam axis component) distributions for fragments with $Z = 6$ and $Z = 8$. The total velocity spectra, normalized to unit area, are shown in black solid lines, while colored dashed lines represent the velocity distributions with primary fragment selection.

Here, we note that these are mainly produced from primary fragments with the same Z, i.e., they are already produced in the dynamic phase of the reaction. With less probability, they are generated in the afterburner from a heavier primary fragment. The different origin of the final fragment reflects in the different velocity spectra: for fragments slightly heavier than the final one, the velocity spectra reflect the velocity distributions of their primary sources, while the heaviest primary fragments correspond to final velocities close to the v_{CM} value.

The major differences between experimental and AMD+GEMINI++ distributions appear (see Figs. 5 and 6) for fragments with $4 < Z < 10$, where the model predicts higher velocities than the measured ones. As a representative case, we can analyze $Z = 6$ and $Z = 8$ fragments, charge values that are those of the target and the projectile nuclei. Again,

in Fig. 9 the total velocity spectra (solid lines), normalized to unit area, and the velocity distributions obtained selecting some different primary fragments (dashed lines) are shown. For Carbon ions the low velocity part of the spectra is produced mainly from the QT while the high velocity part of the spectra comes from the QP, which decays before 500 fm/c ($Z = 6$ primary) or after ($Z = 8$ primary). For oxygen ions the dominant contribution comes from the projectile ($Z = 8$ primary). However, these final ions can be produced also via fusion-like reactions: when the primary source size increases, the final velocities tend to the v_{CM} region and their distribution assumes a more Gaussian shape.

We can conclude that AMD+GEMINI++ contains all the different mechanisms from which these secondary fragments can be produced, but we expect different cross sections with respect to the experimental ones. The failure of AMD+GEMINI++ to give enough fusion-like processes was already pointed out in [20] for the light systems ^{32}S + ^{12}C and ^{20}Ne + ^{12}C at 25 and 50 MeV/nucleon. In particular, in our work the model overpredicts less dissipative collisions, where the QP and QT fragments populate their typical phase-space and perhaps have a rather low excitation energy, producing an extra yield of $Z = 8$ at velocity near the v_{proj} and of $Z = 6$ at velocity under the experimental thresholds. The decay of QP (typically with $Z = 8, 9, 10$ after a kind of stripping reaction on carbon) produces also an extra yield of $Z = 5, 6, 7$ ions with a velocity similar to the original QP.

The tendency of AMD to underpredict fusion processes can be pointed out studying the AMD+GEMINI++ velocity spectra as a function of the impact parameter b, as shown in Fig. 10. The most noticeable observation is that the fragments $Z = 6, 7, 8$ for central collisions ($b = 0$–2) still are emitted in phase-space regions typical of the most peripheral reactions ($b = 6$–8). Only the heaviest fragments ($Z \geqslant 10$) are compatible with fusion-like processes, suggesting that for central collisions the stopping results to be scarce in the model. This effect might be related to the NN cross section, which is one of the parameters of the model. Another aspect
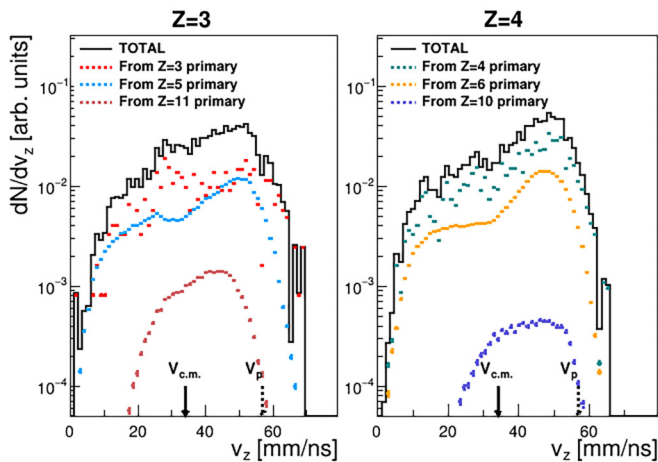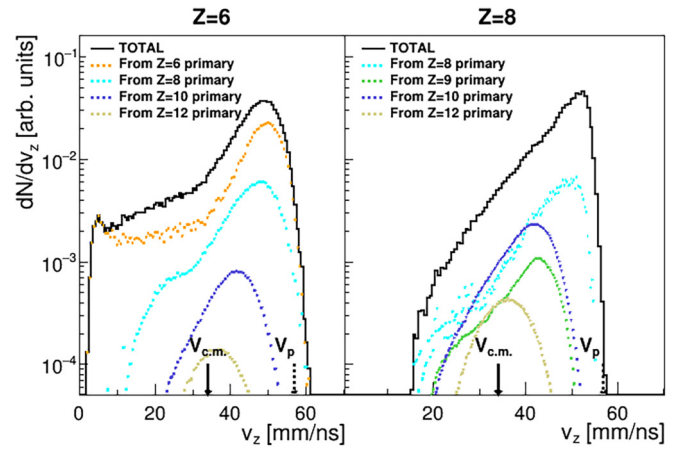

FIG. 8. Model data: laboratory velocity (beam axis component) distributions for fragments with $Z = 3, 4$. The total velocity spectra, normalized to unit area, are shown in black solid lines, while colored dashed lines represent the velocity distributions with primary fragment selection.
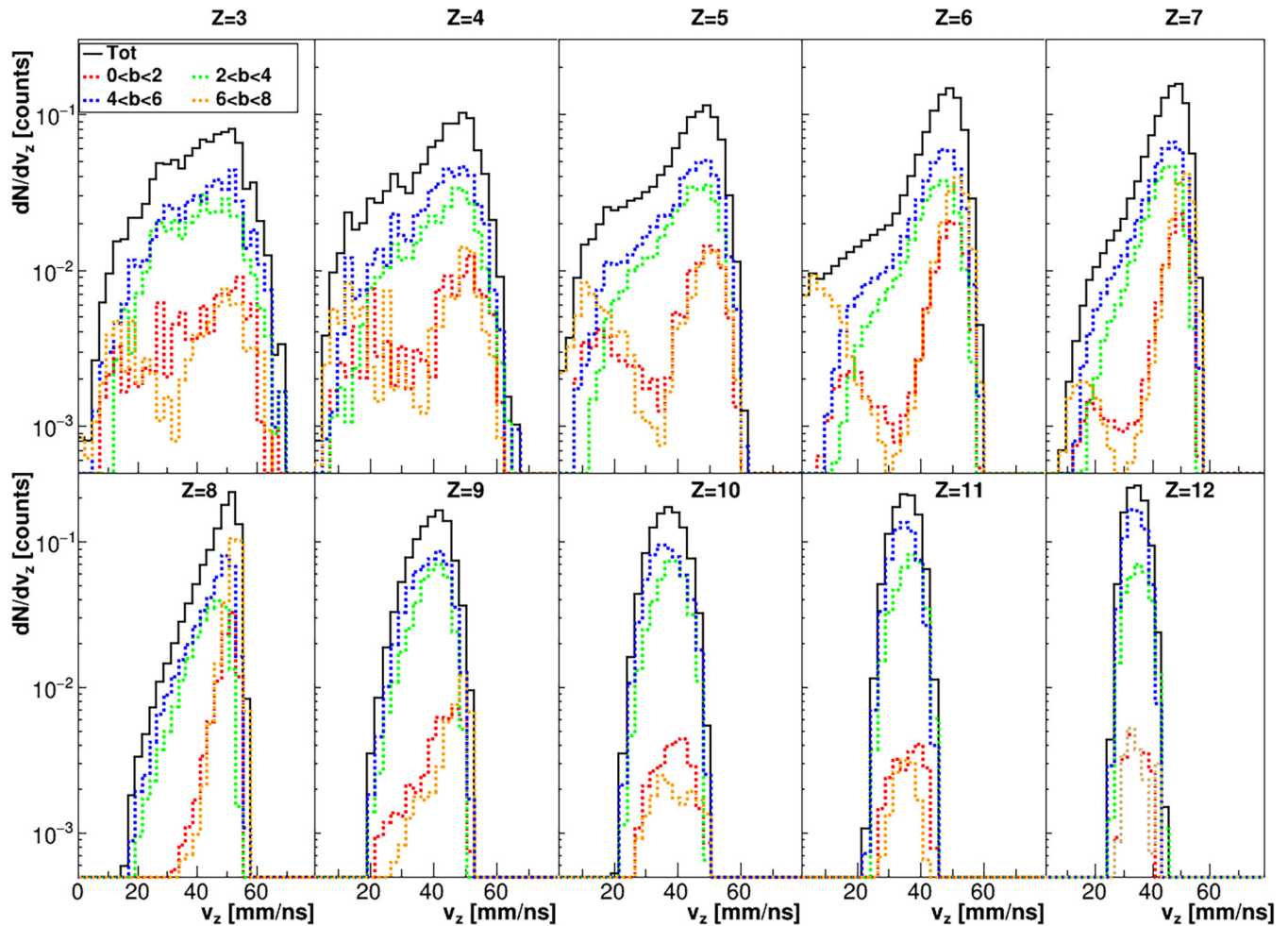
FIG. 10. Model data: laboratory velocity (beam axis component) distributions for secondary fragments with $Z > 2$. The black lines are the total spectra. The colored lines represents the velocity spectra for different selection of the impact parameter b.

that can affect this behavior is the inclusion of the clustering and interclustering interaction: the presence of clusters in an excited configuration may inhibit the interaction between the projectile and target nuclei, producing an extra yield of $Z = 6$ and 8 near the entrance channel velocities. In our analysis, the AMD code has been run with the standard parameters used in [20], but in the future an optimization of the AMD parameter should be performed to better reproduce also light systems with this code.

Considering that for the heaviest fragments $Z = 10$, 11, 12 we can confirm within the model that they are originated from a process of complete/incomplete fusion, we can try to separate those two contributions performing a quantitative comparison between experimental and model data. Starting from the laboratory velocity (beam axis component) of Fig. 6, the two contributions can be highlighted with a two Gaussian fit, as proposed in [39]. As the system is in reverse kinematics and usually the light reaction partner participates only partially in the fusion process [5,35–39], the incomplete fusion is characterized by a velocity larger than v_{CM}. In Fig. 11 the results of the Gaussian fit on the experimental and filtered model spectra are shown. In the fit procedure, we have fixed the mean and the width of the Gaussian which reproduces the complete
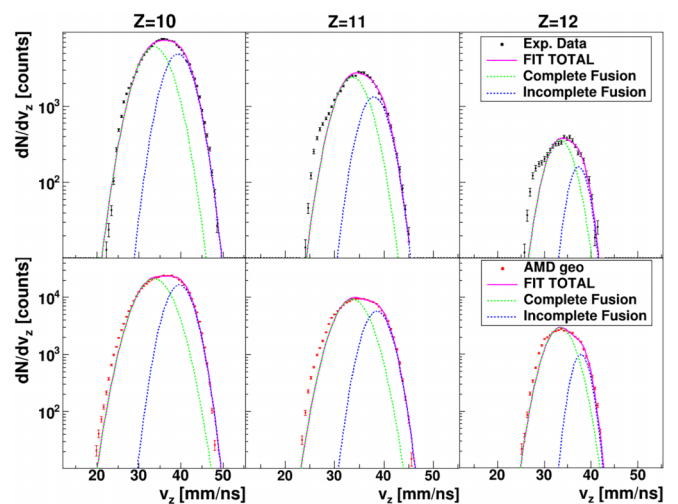

FIG. 11. Laboratory velocity (beam axis component) distributions for experimental (black, upper panel) and AMD+GEMINI++ data (red, lower panel). The magenta solid line is the result of the two Gaussian fit. The green and blue dashed lines represent the complete and incomplete fusion component, respectively.

TABLE I. Results of the Gaussian fit on experimental, filtered and 4π model distributions. For each ion the percentages of complete and incomplete fusion with respect to the total area and their statistical and systematic errors are listed.

		exp (%)	**AMD geo** (%)	**AMD 4pi** (%)
Z=10	CF	$58.5 \pm 0.5 \pm 0.7$	$62.6 \pm 0.3 \pm 1.1$	$53.1 \pm 0.1 \pm 1.3$
	ICF	$40.9 \pm 0.6 \pm 0.8$	$36.7 \pm 0.3 \pm 1.2$	$45.8 \pm 0.1 \pm 1.5$
Z=11	CF	$61 \pm 1 \pm 6$	$64.9 \pm 0.4 \pm 4$	$59.9 \pm 0.1 \pm 4$
	ICF	$34 \pm 1 \pm 5$	$31.8 \pm 0.4 \pm 2$	$36.9 \pm 0.1 \pm 2$
Z=12	CF	$69 \pm 3 \pm 13$	$75 \pm 1 \pm 13$	$74.9 \pm 0.3 \pm 6$
	ICF	$22 \pm 2 \pm 7$	$18.0 \pm 0.7 \pm 6$	$20.8 \pm 0.2 \pm 3$

fusion (green line) at the values suggested by the GEMINI++ code for the compound nucleus of the present reaction, while the parameters of the incomplete fusion Gaussian (blue line) were left free, with the only constraint for the mean to be located at $v > v_{CM}$. In Table I the percentages of complete and incomplete fusion, with respect to the total area, deduced from the fits are listed. In all cases, we have considered a statistical error associated to the fit and a systematic error due to some arbitrariness in the fit limits. Experimental and model data show a similar behavior. Using the 4π simulation, we can also evaluate the impact of the apparatus filter: it results to be negligible for $Z = 12$, while it is sizable for $Z = 10$ and $Z = 11$ perhaps due to a larger effect of the modest coverage of the RCo. The results of the two-Gaussian fit confirm again that ions with $Z \geqslant 10$ are produced in central events, basically associated to fusion-like events. Moreover, the Gaussian fits allow to deduce quantitatively the fractions of complete and incomplete fusion, showing that the experimental ones are rather well reproduced by the AMD+GEMINI++ simulation.

IV. CONCLUSIONS

In this work, we have presented a comparison between experimental data and a transport model simulation for the reaction ^{18}O $+ ^{12}$C at 16.7 MeV/nucleon measured using the GARFIELD+RCo apparatus at LNL. Our analysis has been focused on the $Z > 2$ fragments detected at forward angles $5° < \theta < 17°$.

To our knowledge, for the first time, the AMD transport code has been tested for a light system at a so low bombarding energy. The code is used to mimic the reaction events from the contact time to 500 fm/c; then a statistical code, GEMINI++, is applied as afterburner. with an opportune selection, a comparison of the charge and velocity distribution has been proposed. The general agreement between experimental data and AMD+GEMINI++ is good: the fragments with $Z \geqslant 10$ are expected to be the results of a complete (incomplete) fusion process and the AMD+GEMINI++ model is able to reproduce quite well their multiplicity (except for $Z = 12$), angular and velocity spectra and the fractions of complete and incomplete fusion events. Also the fragments with $Z = 3$ and $Z = 4$ are very well reproduced in terms of multiplicity, angular, and velocity distributions. However a discrepancy emerges from the comparison, with the model underpredicting the very dissipative collisions (fusion type) for most central impacts. This is evidenced by the lack of $Z = 6, 7, 8$ ions with characteristics typical of evaporation residues from very excited compound nuclei. Instead these ions are produced but with seemingly low excitation energy and in phase-space portions close to the entrance channel. A more detailed work should be done on the AMD model to understand if it is possible to better reproduce our experimental data with guided changes of the NN cross section and of the weight of the clustering and interclustering process.

[1] P. Fröbrich, Phys. Rep. **116**, 337 (1984).

[2] W. Hauser and H. Feshbach, Phys. Rev. **87**, 366 (1952).

[3] S. Piantelli, G. Casini, A. Ono, G. Poggi, G. Pastore, S. Barlini *et al.*, Phys. Rev. C **103**, 014603 (2021).

[4] S. Barlini, S. Piantelli, G. Casini, P. R. Maurenzig, A. Olmi, M. Bini *et al.*, Phys. Rev. C **87**, 054607 (2013).

[5] H. Morgenstern, W. Bohne, W. Galster, K. Grabisch, A. Kyanowski *et al.*, Phys. Rev. Lett. **52**, 1104 (1984).

[6] P. Lautesse *et al.*, Eur. Phys. J. A **27**, 349 (2006).

[7] P. Eudes, Z. Basrak, F. Sebille, V. delaMota, G. Royer *et al.*, Phys. Rev. C **90**, 034609 (2014).

[8] D. Dell'Aquila *et al.*, J. Phys. G: Nucl. Part. Phys. **50**, 015101 (2023).

[9] S. Piantelli, S. Valdre, S. Barlini, G. Casini, M. Colonna, G. Baiocco *et al.*, Phys. Rev. C **96**, 034622 (2017).

[10] M. Colonna, M. Di Toro, A. Guarnera, S. Maccarone, M. Zielinska-Pfabe, and H. H. Wolter, Nucl. Phys. A **642**, 449 (1998).

[11] R. Charity *et al.*, Nucl. Phys. A **483**, 371 (1988).

[12] R. J. Charity, Phys. Rev. C **82**, 014610 (2010).

[13] G. A. Souliotis, P. N. Fountas, M. Veselsky, S. Galanopoulos, Z. Kohley, A. McIntosh, S. J. Yennello, and A. Bonasera, Phys. Rev. C **90**, 064612 (2014).

[14] M. Papa, T. Maruyama, and A. Bonasera, Phys. Rev. C **64**, 024612 (2001).

[15] M. Papa *et al.*, J. Comput. Phys. **208**, 403 (2005).

[16] A. Ono *et al.*, Phys. Rev. C **59**, 853 (1999).

[17] S. Piantelli, A. Olmi, P. R. Maurenzig, A. Ono, M. Bini, G. Casini *et al.*, Phys. Rev. C **99**, 064616 (2019).

[18] S. Piantelli, G. Casini, A. Ono, G. Poggi, G. Pastore, S. Barlini *et al.*, Phys. Rev. C **101**, 034613 (2020).

[19] A. Camaiani, G. Casini, S. Piantelli, A. Ono, E. Bonnet, R. Alba *et al.*, Phys. Rev. C **103**, 014605 (2021).

[20] C. Frosin, S. Piantelli, G. Casini, A. Ono, A. Camaiani, L. Baldesi *et al.*, Phys. Rev. C **107**, 044614 (2023).

[21] G. Tian *et al.*, Phys. Rev. C **95**, 044613 (2017).

[22] G. Tian *et al.*, Phys. Rev. C **97**, 034610 (2018).
[23] R. Han, Z. Chen, R. Wada, A. Ono, G. Tian, F. Shi, X. Zhang, B. Liu, and H. Sun, Phys. Rev. C **102**, 064617 (2020).
[24] G. Tian *et al.*, Phys. Rev. C **107**, 044602 (2023).
[25] A. Ono, Prog. Part. Nucl. Phys. **105**, 139 (2019).
[26] M. Bruno *et al.*, Eur. Phys. J. A **49**, 128 (2013).
[27] L. Bardelli *et al.*, Nucl. Instrum. Methods Phys. Res. A **654**, 272 (2011).
[28] P. Ottanelli *et al.*, Il Nuovo Cimento C **42**, 19065 (2019).
[29] N. Ikeno, A. Ono, Y. Nara, and A. Ohnishi, Phys. Rev. C **93**, 044612 (2016).
[30] A. Ono, J. Phys.: Conf. Ser. **420**, 012103 (2013).
[31] D. D. S. Coupland, W. G. Lynch, M. B. Tsang, P. Danielewicz, and Y. Zhang, Phys. Rev. C **84**, 054603 (2011).

[32] C. Ciampi, S. Piantelli, G. Casini, A. Ono, J. D. Frankland, L. Baldesi *et al.*, Phys. Rev. C **108**, 054611 (2023).
[33] C. Ciampi, S. Piantelli, G. Casini, G. Pasquali, J. Quicray, L. Baldesi *et al.*, Phys. Rev. C **106**, 024603 (2022).
[34] A. Camaiani, S. Piantelli, A. Ono, G. Casini, B. Borderie, R. Bougault *et al.*, Phys. Rev. C **102**, 044607 (2020).
[35] Y. Chan, M. Murphy, R. G. Stokstad, I. Tserruya, S. Wald, and A. Budzanowski, Phys. Rev. C **27**, 447 (1983).
[36] G. S. F. Stephans *et al.*, Phys. Lett. B **161**, 60 (1985).
[37] M. F. Vineyard *et al.*, Phys. Rev. C **49**, 948 (1994).
[38] X. Qian *et al.*, Nucl. Phys. A **611**, 370 (1996).
[39] S. Pirrone, G. Politi, G. Lanzalone, S. Aiello, N. Arena, S. Cavallaro, E. Geraci, F. Porto, and S. Sambataro, Phys. Rev. C **64**, 024610 (2001).